Investigation and Simulation of Three–Phase Flow in Porous Media

BY RALF HUBER[a] AND RAINER HELMIG[b]

[a] *Institut für Wasserbau, Universität Stuttgart, Pfaffenwaldring 61, 70569 Stuttgart, Germany*
EMail: r.huber@tu-bs.de
[b] *Institut für Angewandte Mechanik, Fachgebiet für Numerische Methoden und Informationsverarbeitung, Techn. Universität Braunschweig, Pockelsstr. 3, 38106 Braunschweig, Germany*
EMail: r.helmig@tu-bs.de

Abstract

Two full three–phase flow simulators are developed and compared. The first simulator uses the coupled pressure–saturation formulation with a fixed set of primary variables. The second method is based on a variable substitution algorithm with different sets of primary variables dependent on the local phase state: In the absence of a phase the corresponding global mass fraction replaces a phase saturation in the set of primary variables. The system equations are discretized with the same finite volume method – the so–called box–scheme –. The simulators are verified on well–known test problems. By hand of two– and three–dimensional examples three–phase flow in porous media is investigated.

Key words: multiphase flow, finite volume method, porous media, capillary effects.

1 INTRODUCTION

Groundwater contaminations often occur on industrial sites where, e.g., the leakage of storage tanks is not noticed in time, or they are caused by accidental spills. Such accidents quite often happen when hazardous liquids are transported on the road or by train. Safety measures and precautions can reduce the risk of ground and groundwater contaminations. However, if once such an infiltration of NAPL (non–aqueous phase liquids) has taken place it is difficult to have the contaminated site cleaned up.

Contaminants such as petroleum products and other organic compounds which can dissolve in the groundwater are of major concern to the supply of safe drinking water. Some substances are already toxic to human health when consumed in small concentrations. The study of the physical processes which govern the propagation and migration of these hazardous contaminants has significantly increased during recent years. This is due to a higher public attention to such environmental problems. Most studies evolve from earlier work in petroleum engineering where multiphase flow was examined and first numerical simulations had been conducted (e.g., Buckley & Leverett (1942), Gottfried et al. (1966), and Peaceman (1977)).[4,13,26]

In contrast to the conditions in petroleum reservoirs, for groundwater hydrologists and environmental engineers capillary forces are of significant interest. The applications differ considerably in the magnitude of the dominating forces and the spatial dimensions. Reservoirs having dimensions of several kilometers are common. Flow is initiated by enforcing high pressures at the infiltration wells. However, multiphase flow due to groundwater contaminations happens mostly over small distances under natural conditions. Capillary forces which are relatively small play an important role for these processes.

A penetration of NAPL phase into the ground is followed by solution processes which usually take place over a very long period of time. Thus, a plume of contaminated groundwater with significant concentrations of hazardous substances can migrate due to basic groundwater movements in the aquifer large distances from the contaminant source.

There are first attempts to model efficient remediation techniques. Forsyth and Shao (1991) simulated gas venting as a tool for in–situ remediation.[12] Other studies have been carried out by Falta et al. (1992) who investigated steam injection as a means for the removal of contaminants which usually form a nonaqueous phase liquid (NAPL) from the subsurface.[7] Air sparging is another option which is especially attractive for the remediation of dense NAPL (DNAPL) which have a higher density than water in the saturated zone (McCray and Falta (1997)).[23] These are the most popular in–situ remediation techniques. There are many others. All these methods are quite new. Because many physical processes in the subsurface are not fully understood, there is a large potential to improve the present techniques. They are in general either too costly, or they need too long clean–up times. Finally, neither ground and groundwater contaminations nor their successful removal are easy to assess.

In petroleum engineering the fractional flow formulation is very popular because it can be combined with direct solution algorithms (e.g., Chavent and Jaffré (1986), Arbogast et al. (1997)).[1,5] It is generally used with the mixed finite element method and the IMPES (implicit pressure–explicit saturation)–time discretization concept. This concept is applicable when capillary processes are of minor importance. However, if capillary forces are dominant an iterative solution algorithm becomes necessary (e.g., Huber (1995), Huber & Helmig).[18,19]

Many multiphase flow simulations are carried out with major simplifications to the physics. For example, in the vadose zone it is common to assume a static air phase (e.g., Richards

(1931), Faust (1985)).[8,27] This assumption is valid for shallow aquifers and it makes the air phase conservation equations redundant. Other models neglect the pressure dependency of various quantities, e.g., porosity, fluid densities, or viscosities. These simplifying assumptions lead to more efficient calculations. However, they are not applicable to a wide range of problems.

To contribute to a better understanding for multiphase flow and transport processes the multi–phase multi–component simulation program system $MUFTE-UG$ is developed. $box3p$ and $box3p3c$ are full three–phase flow formulations which are integrated into $MUFTE-UG$. They are developed from the two–phase formulation $box2p$ which has been used for various studies of NAPL migration in the saturated zone of homogeneous as well as strongly heterogeneous porous media (Helmig (1997), Helmig & Huber, Huber & Helmig).[15,16,19] $MUFTE-UG$ constitutes a computer architecture which allows for multigrid and parallel computations.

This paper has the following structure: In Section 2, from the governing equations two mathematical formulations of multiphase flow in porous media are derived. Then in Section 3 the numerical formulations of the three–phase simulators $box3p$ and $box3p3c$, which are both based on the finite volume method (box scheme), are presented. In Section 4 the two simulators are verified using different three–phase Buckley–Leverett problems. For this class of problems quasi–analytical solutions are known. Two– and three–dimensional NAPL infiltration problems which are typical for accidental spills of hazardous substances on the ground surface are simulated and investigated in the fifth section. Finally, the numerical results from Sections 4 and 5 are discussed and future developments of the simulators are mentioned.

2 GOVERNING EQUATIONS AND MATHEMATICAL FORMULATIONS

Three–phase systems in the subsurface typically consist of two liquid phases (water (w) and a non–aqueous phase liquid (n), in short NAPL) and one gazeous phase (g) which is in most cases air. Conservation of each phase $\alpha \in \{w,n,g\}$ is described by the following continuity equations:[26]

$$\frac{\partial(\phi\,\rho_\alpha S_\alpha)}{\partial t} \quad = \quad -\nabla\cdot[\rho_\alpha v_\alpha]+q_\alpha \quad ,\alpha\in\{w,n,g\} \quad , \tag{1}$$

where S_α, ρ_α, v_α, q_α is the saturation, the density, the Darcy velocity, the mass source rate of each phase α, respectively, and ϕ is the porosity.
Flow in porous media generally occurs at very small velocities where Darcy's law is valid. The original Darcy's law which is formulated for single–phase flow can be generalized to multiphase flow through introduction of the concept of relative permeability. The relative permeability is considered a function of the saturations which accounts for the interaction of simultaneous flow and obstruction within the porous medium between the individual phases. The Darcy velocity of each phase α is given by

$$v_\alpha = -\lambda_\alpha\,\mathbf{K}\,(\nabla p_\alpha - \rho_\alpha g) \quad ,\alpha\in\{w,n,g\} \quad , \tag{2}$$

where $\lambda_\alpha = k_{r\alpha}/\mu_\alpha$ is the mobility of phase α – the quotient of relative permeability and dynamical viscosity. $\mathbf{K}$ denotes the absolute permeability tensor, p_α is the phase pressure, and g is the gravitational acceleration vector.
The saturations obey the following constraint everywhere and everytime:

$$S_w + S_n + S_g = 1 \quad . \tag{3}$$

Because the phases are assumed to be immiscible, interfaces develop between the different phases. The difference of phase pressures at these interfaces is the corresponding capillary pressure, i.e.,

$$p_{c\alpha\beta} = p_\alpha - p_\beta \quad , \tag{4}$$

where α is the non–wetting phase having the higher phase pressure. Capillary pressure–saturation relationships[8,25] are strongly non–linear functions of the saturations. One concept to describe them in a three–phase system is given in the following section.
In three–phase systems the following functional dependency of the relative permeabilities have been observed in experiments:[2,30]

$$k_{rw} = k_{rw}(S_w)\,, \quad k_{rn} = k_{rn}(S_w,S_g)\,, \quad k_{rg} = k_{rg}(S_g) \quad . \tag{5}$$

The NAPL relative permeability–saturation function k_{rn}, usually, is constructed from two–phase data using scaling methods after Stone, Aziz and Settari.[2,30]
Substitution of the Darcy velocity from equation (2) into the continuity equation (1) yields

$$\frac{\partial(\phi\rho_\alpha S_\alpha)}{\partial t} \quad = \quad \nabla\cdot[\rho_\alpha\lambda_\alpha\,\mathbf{K}\,(\nabla p_\alpha - \rho_\alpha g)]+q_\alpha \quad , \quad \alpha\in\{w,n,g\} \quad . \tag{6}$$

These differential equations are the basis of the multiphase simulators *box*2*p* (for two–phase systems) and *box*3*p* (for three-phase systems) which will be derived in the following section. By introduction of global mass fractions Z_α for each phase α and the following equality

$$\phi \rho_\alpha S_\alpha = \phi Z_\alpha \sum_\beta \rho_\beta S_\beta \quad , \tag{7}$$

the system equations of the three–phase simulator *box*3*p*3*c* are derived by substitution of (7) into (6):

$$\frac{\partial(\phi Z_\alpha \sum_\beta \rho_\beta S_\beta)}{\partial t} = \nabla \cdot [\rho_\alpha \lambda_\alpha \mathbf{K} (\nabla p_\alpha - \rho_\alpha g)] + q_\alpha \quad , \alpha \in \{w, n, g\} \, . \tag{8}$$

3 NUMERICAL FORMULATION

For the numerical simulation of three–phase flow a finite volume technique is applied to the differential equations (6) and (8), respectively. The finite volume method (box scheme) can be derived with the principle of weighted residuals. Equations (6) can be weakly formulated with piecewise constant test functions

$$W_i = \begin{cases} 1 & \text{in box } B_i \\ 0 & \text{otherwise} \end{cases} \quad , \tag{9}$$

and shape functions N_i for pressures and saturations, which are linear for triangular and bilinear for quadrilateral elements. Each box is associated with a node, and vice versa. The resulting integral equations are

$$\int_\Omega W_i \frac{\partial(\phi \rho_\alpha \tilde{S}_\alpha)}{\partial t} dx = \int_\Omega W_i \nabla \cdot [\rho_\alpha \lambda_\alpha \mathbf{K} (\nabla \tilde{p}_\alpha - \rho_\alpha g)] \, dx + \int_\Omega W_i q_\alpha dx \quad , \quad \alpha \in \{w, n, g\} \quad , \tag{10}$$

where $\tilde{p}_\alpha = \sum_i p_{\alpha i} N_i$ and $\tilde{S}_\alpha = \sum_i S_{\alpha i} N_i$ are the approximations to pressure p_α and saturation S_α, respectively. $p_{\alpha i}$ and $S_{\alpha i}$ are the nodal values. The i under the summation in (10) implies a sum over all nodes.
Applying Green's formula gives

$$\int_{B_i} \frac{\partial(\phi \rho_\alpha \tilde{S}_\alpha)}{\partial t} dx = \int_{\partial B_i} [\rho_\alpha \lambda_\alpha \mathbf{K} (\nabla \tilde{p}_\alpha - \rho_\alpha g)] \cdot \vec{n} \, ds + \int_{B_i} q_\alpha dx \quad , \quad \alpha \in \{w, n, g\} \quad , \tag{11}$$

where $\vec{n}$ is the outward unit normal. The discrete fluxes are represented by the boundary integrals of each box B_i. This yields a locally mass conservative scheme. In the case of rectangular elements the scheme represents a 5–point stencil.
Typically, the water phase is the wetting phase, and NAPL the intermediate wetting phase of the three–phase system water–NAPL–gas.
For the three–phase capillary pressures the common conceptual model is assumed which says that in the presence of all three phases a NAPL film is situated between the gas and water phases which prevents the development of gas–water interfaces. This conceptual approach is supported by recent micromodel observations by Keller et al.[20] who concluded that generally there do not form water–gas interfaces in a three–phase system. However, for small NAPL saturations, this assumption becomes invalid and a scaling after Forsyth (1991) is employed in order to have a continuous transition from the three–phase to the two–phase relations, and vice versa.[10] Then the phase pressures are of the following form:

$$p_g = p_n + \Theta \, p_{cgn}(S_g) + (1 - \Theta) \, [p_{cgw}(S_w) - p_{cnw}(S_w = 1)] \tag{12}$$

$$p_n = p_w + \Theta \, p_{cnw}(S_w) + (1 - \Theta) \, p_{cnw}(S_w = 1) \tag{13}$$

where $p_{cgw} = p_{cgw}(S_w)$, $p_{cnw} = p_{cnw}(S_w)$, $p_{cgn} = p_{cgn}(S_g)$ are the two–phase capillary pressure functions. Scaling parameter Θ is given by

$$\Theta = \min(1, S_n/S_{nr}) \quad . \tag{14}$$

By application of a backward Euler time discretization and mass lumping of the accumulation terms, the discrete formulation can be written as follows:

$$\mathcal{L}_{\alpha i} := \frac{|B_i|}{\Delta t}\left\{[\phi\,\rho_\alpha S_\alpha]_i^{t+\Delta t} - [\phi\,\rho_\alpha S_\alpha]_i^{t}\right\} \\ - \sum_{j\in\eta_i}(\rho_\alpha\lambda_\alpha)_{ups(i,j)}\,\gamma_{\alpha ij} - |B_i|\,q_{\alpha i} \quad = 0 \quad , \quad \alpha\in\{w,n,g\} \quad , \tag{15}$$

where η_i is the set of all neighbor boxes which have a mutual box boundary face with box i, or in other words, all indices j with $|\gamma_{\alpha ij}| > 0$. $|B_i| = \int_{B_i} dx$ is the volume of box B_i. The transmissivity integral/term for the box scheme which represents the discrete flux between neighboring boxes is given by

$$\gamma_{\alpha ij} = -\sum_{e:i,j\in e}\left[\mathbf{K}\,(\nabla\tilde{p}_\alpha - \rho_\alpha\,g)\right]_{|x=P^e_{ij}}\cdot\vec{n}(l^e_{ij})\,A(l^e_{ij}) \quad . \tag{16}$$

Each quadrilateral element is divided into four subcontrol–volumes each of which belongs to a box associated with an element node. The term in brackets in (16) is evaluated at the midpoint P^e_{ij} of the dividing line l^e_{ij} between the two subcontrol–volumes of the boxes i and j inside of element e (see Fig. 1). $A(l^e_{ij})$ is the area of this box boundary segment.
The mobilities and densities in the flux term are upstream weighted. The α–phase upstream direction at the interface between boxes i and j is determined by

$$ups(i,j) = \begin{cases} i & \text{if} \quad \gamma_{\alpha ij} \geq 0 \\ j & \text{if} \quad \gamma_{\alpha ij} < 0 \end{cases} \quad . \tag{17}$$

This upstream weighting of saturation dependent terms is necessary to obtain a stable solution, especially in the case of convection–dominated processes where the equations are essentially hyperbolic.
The discrete phase conservation equations for the *box3p3c* simulator are obtained analogously and have the following form:

$$\mathcal{L}_{\alpha i} := \frac{|B_i|}{\Delta t}\left\{\left[\phi Z_\alpha\sum_\beta(\rho_\beta S_\beta)\right]_i^{t+\Delta t} - \left[\phi Z_\alpha\sum_\beta(\rho_\beta S_\beta)\right]_i^{t}\right\} \\ - \sum_{j\in\eta_i}(\rho_\alpha\lambda_\alpha)_{ups(i,j)}\,\gamma_{\alpha ij} - |B_i|\,q_{\alpha i} \quad = 0 \quad , \\ \alpha\in\{w,n,g\} \quad . \tag{18}$$

In the case of the two–phase simulator *box2p* the primary variables are fixed over the entire model domain and numerical simulation. They are either (p_w, S_n) or (S_w, p_n). The three–phase simulator *box3p* uses as primary variables two phase saturations and the phase pressure of the third phase, and they are fixed for the entire simulation, i.e., the set of primary variables is one out of the following set of triplets: $\{(p_w, S_n, S_g), (S_w, p_n, S_g), (S_w, S_n, p_g)\}$.
In contrast to the first two methods the choice of primary variables for *box3p3c* depends on the set of phases resident at the corresponding location (box) during the numerical simulation. Table 1 shows for each possible phase state (combination of resident phases) the corresponding set of primary variables. $V_{\alpha i}$ is the (nodal) primary variable associated with the α–phase conservation equation $\mathcal{L}_{\alpha i}$ for box B_i. A variable substitution is done in the case of a local

Table 1: Phase states and primary variables of *box3p3c*

Resident Phases	Primary Variables		
	V_w	V_n	V_g
water, NAPL, gas	S_w	S_n	p_g
water, NAPL	Z_g	S_n	p_g
NAPL, gas	Z_w	S_n	p_g
water, gas	S_w	Z_n	p_g
water	Z_g	Z_n	p_g
NAPL	Z_w	Z_g	p_g
gas	Z_w	Z_n	p_g

phase appearance or disappearance. These transitions are recognized when during the iteration process negative saturations appear, or when the global mass fraction of an absent phase becomes positive.

All discussed multiphase simulators utilize the Newton–Raphson concept to solve the discrete system equations. The Jacobian is constructed with a chord slope technique. The partial derivatives can be obtained either by central or by backward finite difference approximations. The numerical differentiation has then in the case of the central difference approximation of the slopes the following form:

$$\partial_{\beta j}\mathcal{L}^e_{\alpha i} := \frac{\mathcal{L}^e_{\alpha i}(V_{\beta j}+\delta_{\beta j}) - \mathcal{L}^e_{\alpha i}(V_{\beta j}-\delta_{\beta j})}{2\delta_{\beta j}} \quad , \tag{19}$$

where $\mathcal{L}^e_{\alpha i}$ is the contribution of element e to the expression $\mathcal{L}_{\alpha i}$ (eq. (15) and (18), respectively), and $\delta_{\beta j}$ is the variation in primary variable $V_{\beta j}$ by a value of $\delta_{\beta j} = \varepsilon |V_{\beta j}| + \varepsilon$ where ε is a very small number. ε guarantees that the denominator of expression (19) is bounded from below. Here, ε was assigned a value of 10^{-9}.

With the use of the following short notation

$$\partial_\beta \mathcal{L}^e_\alpha := \left[\partial_{\beta j}\mathcal{L}^e_{\alpha i}\right]_{i,j\in e} \tag{20}$$

the element Jacobian matrix can be expressed as

$$J^e = \begin{bmatrix} \partial_w \mathcal{L}^e_w & \partial_n \mathcal{L}^e_w & \partial_g \mathcal{L}^e_w \\ \partial_w \mathcal{L}^e_n & \partial_n \mathcal{L}^e_n & \partial_g \mathcal{L}^e_n \\ \partial_w \mathcal{L}^e_g & \partial_n \mathcal{L}^e_g & \partial_g \mathcal{L}^e_g \end{bmatrix} \quad . \tag{21}$$

Convergence for each time iteration is recognized when changes in the unkowns are less than 10^{-10} in the max–norm. Has this not been achieved within 6 newton iterations a time–step reduction by one half is done. When the tolerance is reached within two iterations a time step doubling is employed.

For the solution of the resulting systems of linear equations there is a variety of solvers available. Since *box2p* and *box3p* have fixed primary variables these two methods can be combined with multigrid schemes. For the *box3p3c* simulator an option to speed up the algorithm could be the use of an adaptive–implicit time discretization (Forsyth (1989)).[9] This method eliminates at nodes which satisfy a certain stability criterium the saturations as primary variables in

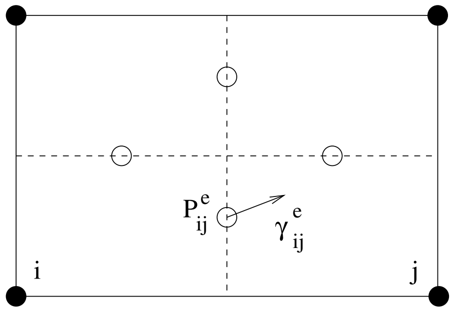

Figure 1: Box discretization for a rectangular element *e*

the linear system of equations. They are calculated in a postprocessing procedure by use of an IMPES (implicit pressure–explicit saturation)–concept.
In the following computations the (S_w, S_n, p_g)–primary variable set is employed for the *box3p* formulation. For both methods the BICGSTAB matrix solver is used.

4 VERIFICATION

One special case of three–phase flow in porous media is the so–called three–phase Buckley–Leverett (BL) problem. It is an extension to the original (two–phase) Buckley–Leverett problem. This problem describes the immiscible displacement of the resident phases by one phase which usually is water. This process is typical for secondary and tertiary oil recovery techniques of subsurface reservoirs by means of water flooding.[13] Here, in the four presented examples which have been adopted from Gottfried et al. (1966), water displaces either a combination of oil and residual water, or, a combination of oil, residual water and free gas. Gravity, capillary and compressibility effects are ignored.
An extension to this model is the black–oil model where dissolved gas in the oil phase is taken into account (see Peaceman (1977)).[26] Bell et al. (1986) discovered that the three–phase Buckley–Leverett differential equations contain an elliptic region within the phase saturation domain, which is of interest for the choice of solution methods to be employed.[3] Gottfried et al. (1966) studied the influence of the initial saturation distribution of oil reservoirs on the displacement process through water flooding and the recovery rates of oil.[13]
The model domain is of dimension $L = 0.9144m (= 3ft)$. Water is injected at one end with a constant flow rate of $q_w = 2.94 \cdot 10^{-4} kg\, m^{-2}\, s^{-1}$. For the discretization an equidistant grid with 120 (two–dimensional square) elements and a grid size of $\Delta x = 0.00762m$ is used.
Fig. 2 shows the initial and boundary conditions of the problem. At the left boundary a water saturation of $S_w = 1$ is assumed throughout the simulation. During the numerical simulation this was weakly enforced by an initial water saturation of 1 at the corresponding boundary boxes, and a no–flow boundary for the remaining phases. Since flow is enforced from left to right (see Fig. 2) a pressure gradient is build up which prevents the other phases from flowing upstream.
The relative permeabilities are given by:

$$
\begin{aligned}
k_{rw} &= \bar{S}_w^4 && (22)\\
k_{rn} &= \left(1 - \bar{S}_g - \bar{S}_w\right)^3 \left(1 - \bar{S}_g + \bar{S}_w\right) && (23)\\
k_{rg} &= \bar{S}_g^3 \left(2 - \bar{S}_g\right) && (24)
\end{aligned}
$$

where $\bar{S}_w = (S_w - S_{wr})/(1 - S_{wr})$, $\bar{S}_g = S_g/(1 - S_{wr})$, $S_w \leq S_{wr}$. Equation (23) describes in the case of residual water saturation a Corey–type relative permeability–saturation curve.[17] Here, the water residual saturation is $S_{wr} = 0.20$. It should be noted that these constitutive relationships are different from the ones encountered in groundwater contamination and remediation scenarios.
The fluid properties are given in Table 2. Initial conditions and the porosity for each of the four example problems are listed in Table 3. The initial saturations are valid throughout the entire flow domain.
Techniques by Welge,[31] Buckley and Leverett[4] can be used in such special cases to obtain quasi–analytical solutions. They yield for the first BL problem a front saturation of $S_w^* = 0.40$ and a front velocity of $v_{wn} = 0.50m/d$. Behind the shock front a rarefaction wave forms.
An initial time step of $\Delta t = 360s$ was used. Fig. 3–6 display the numerical results after 12, 24, and 36 hours of water flooding. The solid lines correspond to the water, the dotted ones to the oil, and the dashed ones to the gas saturation profiles.
The second example represents a three–phase system. The results show that two shock fronts

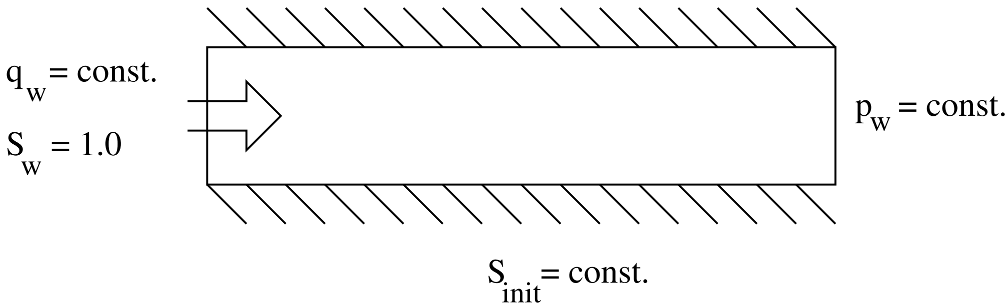

Figure 2: Configuration of the Buckley–Leverett Problem

Table 2: Fluid properties

Parameter	Unit	Water	Oil	Gas
Viscosity	$kg/(m\ s)$	$8 \cdot 10^{-4}$	0.265	$2 \cdot 10^{-5}$
Residual saturation	–	0.20	0.00	0.00

develop which propagate at different speeds. At first oil displaces gas, which has a much lower viscosity and is therefore very mobile. The predicted characteristic values of this front by quasi–analytical methods are $S_n^* = 0.79$ and $v_{ng} = 0.44 m/d$. A slower front lags behind this first front. Here, water essentially displaces oil at a predicted velocity of $v_{wn} = 0.31 m/d$ and a front saturation of $S_w^* = 0.42$. An oil bank develops between the two propagating shock fronts. The initial saturations differ in the third example from the second by a slightly lower oil saturation S_n and a slightly higher water saturation S_w. The result resembles the one from the preceding example. However, the propagation speeds of the two fronts are now closer to each other ($v_{ng} = 0.44 m/d$ and $v_{wn} = 0.40 m/d$). As a result the oil bank develops much slower, and during the simulation a peak of $S_n^* = 0.74$ forms. The water front moves with a front saturation of $S_w^* = 0.40$. The interesting point of this problem lies in the difficulty for a numerical scheme to reproduce the peak accurately. Sleep and Sykes[29] used this third case as a verification for their code. They compared one–point and two–point schemes with a third–order upstream weighting method and concluded that the second method gave the best results. The last method gave entropy–violating shocks.

If now the initial water saturation is still increased at the expense of the oil saturation, the quasi–analytical methods predict under the assumption of moving oil–gas and water–oil fronts that the water–oil displacement occurs at a higher velocity than the propagation of the oil–gas front. The predicted values are: $v_{wn} = 0.59 m/d$ and $v_{ng} = 0.43 m/d$. However, these values imply a displacement process which differs from the one these predictions were based on. Consequently, the numerical simulation yields a different scenario: No oil bank forms. Instead there is only one displacement front, where water essentially displaces gas. Its velocity can be calculated by quasi–analytical means to have a value of $v_{wg} = 0.45 m/d$ and a front saturation of $S_w^* = 0.49$.

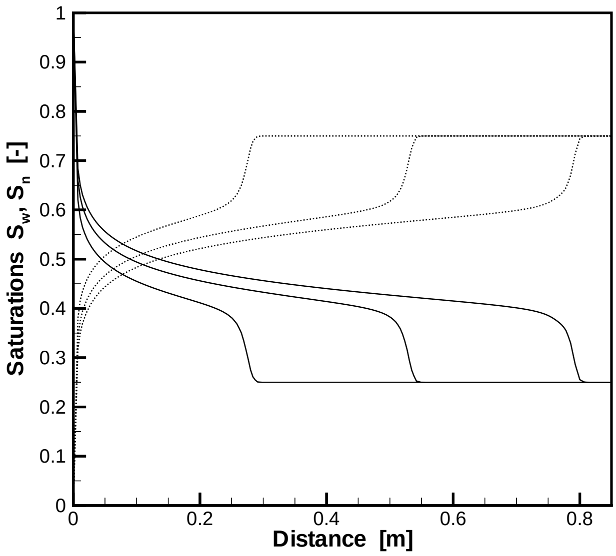

Figure 3: Buckley–Leverett Problem 1

The numerical solutions of the three–phase simulator as depicted in Fig. 3–6 show a very good agreement with the data obtained from quasi–analytical solution techniques.

Table 3: Problem specification

BL problem	No. of phases	ϕ	$S_{w,init}$	$S_{n,init}$	$S_{g,init}$
1	2	0.25	0.25	0.75	0.00
2	3	0.30	0.20	0.60	0.20
3	3	0.30	0.25	0.55	0.20
4	3	0.30	0.30	0.50	0.20

The possible solutions to the corresponding differential equations can be derived from coherence theory (see Helfferich (1981)).[14]

In Table 4 runtime statistics are presented for the four problems. Here, the runtimes for *box*3*p* are given. The values for *box*3*p*3*c* are almost identical. This comes from the fact that the entire domain is three–phase with the exception of the left boundary. For full three–phase flow the primary variables are the same for both simulators. The cpu time per Newton step behaves like the dimension of the system of equations, i.e., the three–phase formulation takes 1.5 times more cpu time per Newton step than the two–phase formulation. However, the number of Newton steps is 10 percent less for the three–phase simulator. If we compare the total cpu times of the three–phase simulator to solve the four BL–problems, we see that the two–phase problem takes about 2/3 of the runtime required for the three–phase problems. The runtimes for the three–phase problems correlate with the numerical difficulty of the individual problem. The last BL–problem takes less time than the other two, because there is no oil bank forming.

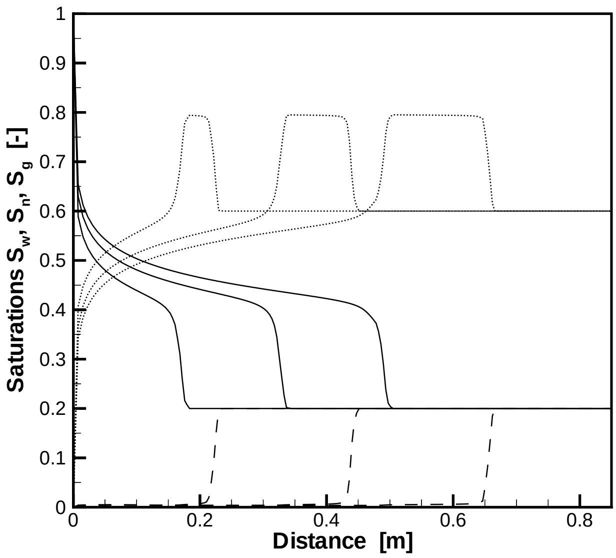

Figure 4: Buckley–Leverett Problem 2

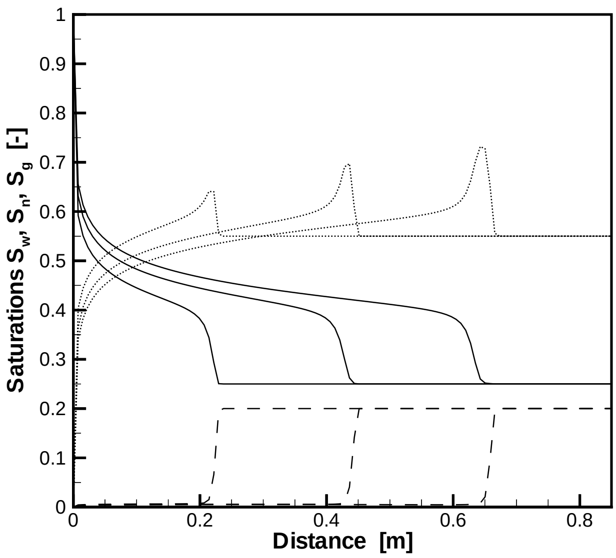

Figure 5: Buckley–Leverett Problem 3

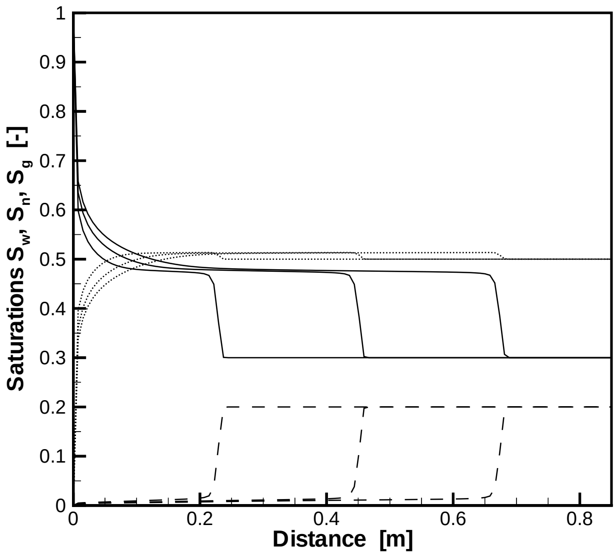

Figure 6: Buckley–Leverett Problem 4

The most time is necessary to solve the third problem. Here, the oil bank represents a high peak which is difficult to resolve. Furthermore, steep saturation gradients occur.

Table 4: Runtime statistics

Parameter	Unit	BL problem				
		1#	1	2	3	4
Total cpu time*	s	15811	21654	30631	31043	27984
No. of time steps	-	361	362	361	361	361
No. of Newton steps	-	1084	998	1408	1424	1283
Cpu time per Newton step*	s	14.6	21.7	21.7	21.8	21.8

: with the two–phase simulator *box2p*;

* : on a Pentium MMX 233 MHz.

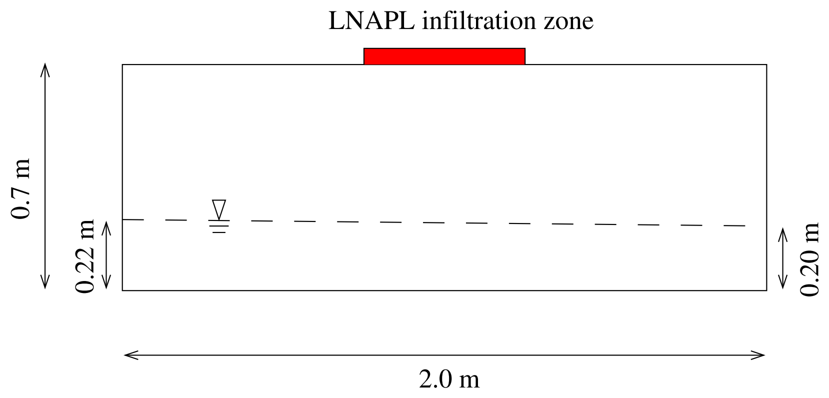

Figure 7: 2D–LNAPL infiltration: Configuration

5 EXAMPLES

5.1 Two–dimensional simulation of LNAPL infiltration into an aquifer with an inclined water table

The simulators *box*3*p* and *box*3*p*3*c* are applied to the following two–dimensional LNAPL infiltration problem: The model domain has a horizontal length of 2.0 m and a vertical length of 0.7 m. At the bottom a water pressure is prescribed which varies linearly from 102158.2 Pa (at the left boundary) to 101962 Pa (at the right boundary). The upper model boundary is a Dirichlet boundary for the air phase pressure with p_g = 100000 Pa. The left and right sides of the model domain are no–flow boundaries. The initial water table is located at the left side 0.22 m and on the right side 0.20 m above the lower model boundary (see Fig. 7). At the beginning of the LNAPL infiltration is the system in an equilibrium state. The infiltration zone is located in the middle of the upper model boundary with a length of 0.5 m. The infiltration rate is $3 \cdot 10^{-6}$ kg/m/s. The fluid and soil properties are given in Tab. 5. Compressibilities of water and NAPL phases are neglected. The soil is assumed to be rigid, i.e., the porosity is constant ($\phi = const.$). Constitutive relationships are taken from Forsyth (1993)[11] in tabulated form and are given in the appendix as Tab. 9 and 10.
The model domain is discretized with a uniform mesh of grid size $\Delta x = \Delta z = 0.10m$. The simulation is done with an initial time step of 1000 s. A maximum time step of 10 days is allowed.
The infiltrating NAPL phase forms a plume which moves downwards through the unsaturated zone due to gravitational forces. After approximately 68 days LNAPL has reached the water table at an elevation 0.21 m above the lower model boundary (see Fig. 8). In Fig. 8 the numerical simulation results of *box*3*p* are illustrated. The dashed line marks the location of the water table. Until this time no significant deformation of the LNAPL plume is observed. The lighter than water LNAPL (850 kg/m^3) does not penetrate the saturated zone. Now a major horizontal movement of the LNAPL phase is starting. The LNAPL plume is spreading in the right direction. However, Figures 8 indicate the existence of a smaller horizontal movement of LNAPL to the left, i.e., upstream – in the counter–direction of the basic groundwater movement.

Table 5: Parameter values for the 2D–LNAPL infiltration problem

Parameter	Symbol	Unit	Value
Permeability	$\mathbf{K}$	m^2	10^{-12}
Porosity	ϕ	–	0.3
Water density	ρ_w	$kg\,m^{-3}$	1000
LNAPL density	ρ_n	$kg\,m^{-3}$	850
Air density	ρ_g	$kg\,m^{-3}$	1.16
Water viscosity	μ_w	$kg\,m^{-1}\,s^{-1}$	10^{-3}
LNAPL viscosity	μ_n	$kg\,m^{-1}\,s^{-1}$	$2.21 \cdot 10^{-3}$
Air viscosity	μ_g	$kg\,m^{-1}\,s^{-1}$	$2 \cdot 10^{-5}$

The motion of LNAPL is an overlapping of several physical processes. There are pressure, gravitational, buoyancy, and capillary forces which affect the movement of the LNAPL plume. Gravity and buoyancy exert forces exclusively vertically downwards and upwards, respectively.
Near the infiltration zone gravitational forces dominate. This is because in the upper unsaturated zone is only water at residual saturation. Within the capillary fringe close to the water table buoyancy forces prevent LNAPL from penetrating further downwards into the saturated zone. Here, flow is mainly controlled by horizontal forces. Pressure forces due to the pressure gradient within the system (which results in an inclined water table) induce a movement of the LNAPL plume to the right (downstream). However, capillary forces act in all directions, and for a small portion of LNAPL these forces induce a movement upstream, i.e., to the left. This result is in agreement with observations of various laboratory experiments and in the field where LNAPL was detected upstream of an infiltration zone (e.g., Sheta et al.[28]). Such propagation processes which occur opposite the main flow direction can be amplified through the presence of small– and large–scale heterogeneities (e.g., Kueper & Frind (1991)), or fractures.[21,22]

Table 6: Runtime statistics (simulation of 130 days)

Parameter	Unit	Formulation	
		box3p	*box3p3c*
Total cpu time*	s	38455	52690
No. of time steps	-	1998	2383

* : on a Pentium MMX 233 MHz.

The numerical results of *box3p3c* are similar to *box3p*. The runtimes listed in Tab. 6 show that the *box3p* formulation has a better convergence behavior and as a consequence a higher computational efficiency than *box3p3c*.

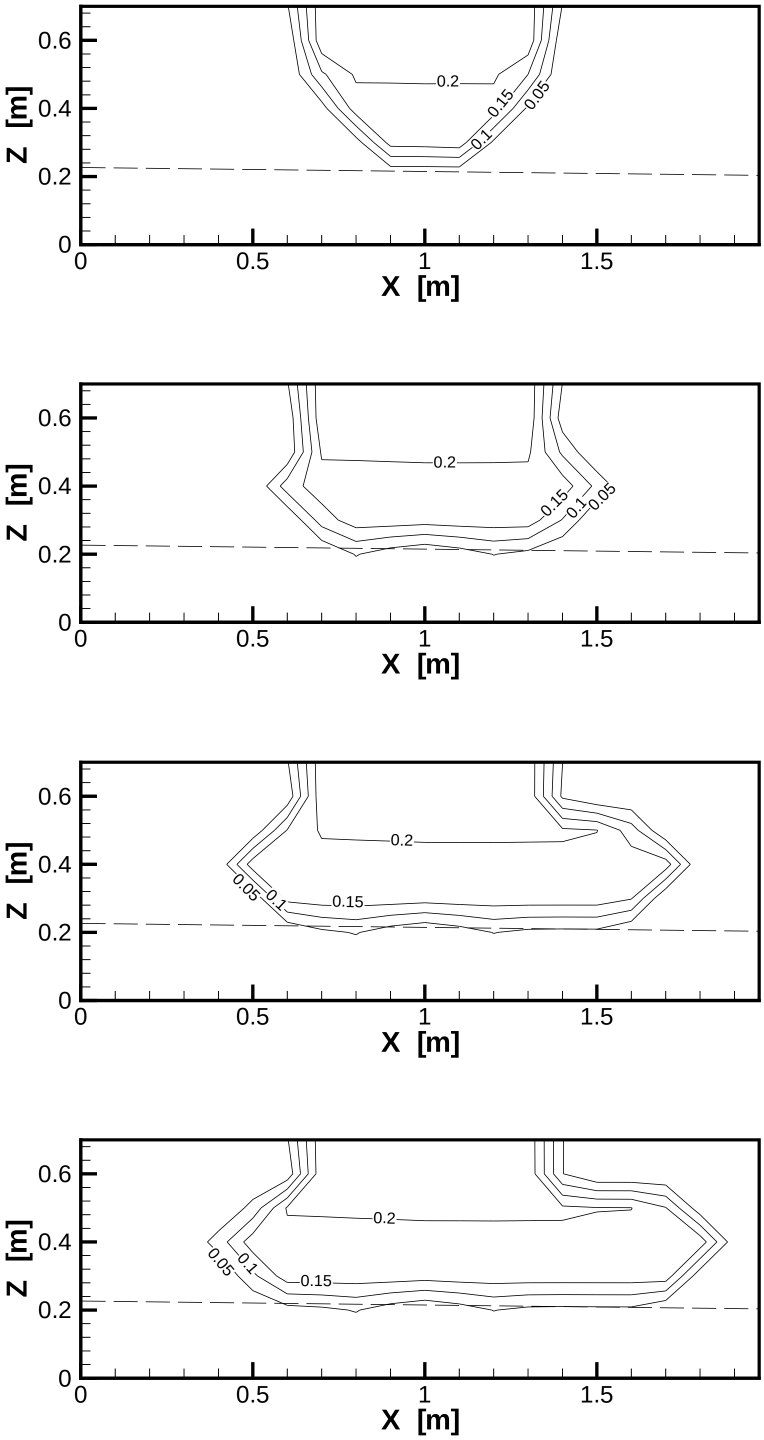

Figure 8: Predicted LNAPL saturations after 68, 91.5, 118, and 130 days of infiltration

5.2 Cross–sectional analysis of NAPL infiltration

This problem describes the movement of a nonaqueous phase liquid (NAPL) in the unsaturated–saturated zone due to an infiltration over a small portion of the ground surface. Because the considered porous medium is assumed to be an aquitard, a basic horizontal movement of groundwater can be neglected. If we assume a homogeneous, isotropic soil this problem becomes axi–symmetric with respect to the vertical axis through the infiltration zone. Thus, it suffices to investigate a vertical cross–section of a cylindrical domain. The considered cross–section covers a horizontal distance of 16.9m from the infiltration zone and a depth of 6 m. Initially, the water table is situated 3 m below the ground surface (see Fig. 9).

Along the ground surface (top boundary) water is continually infiltrating at a rate of $2.54 \cdot 10^{-5} kg/m^2/s$ which corresponds to an annual average recharge of 800mm. Atmospheric pressure is prescribed at the entire top boundary except for the infiltration area. The aquitard is assumed to be underlain by a draining aquifer. A constant pressure head of 129400 Pa is prescribed at the bottom. On the left side no–flow is prescribed because of symmetry reasons. The right boundary is assumed to be far away from the NAPL infiltration zone that it can be assumed to be impermeable.

The initial conditions are obtained from a fully saturated model domain which was allowed to reach a quasi–equilibrium state. Then NAPL starts to infiltrate with a constant volumetric rate of $1.0 m^3$ per year at the upper left corner of the cross–section (center of the considered cylindrical domain).

The porous medium properties are given in Tab. 7. They correspond to a medium sand. The fluid properties are also given in Tab. 7. The two–phase relative permeability–saturation and capillary pressure–saturation data are taken from Forsyth (1993) in tabulated form[11] with one exception: The gas phase relative permeability is assumed to have the following form:

$$k_{rg} = S_g^2 \qquad . \tag{25}$$

We assume a critical and residual NAPL saturation of $S_{nr} = 0.10$ and a water residual saturation of $S_{wr} = 0.20$.

The three–phase constitutive relations are constructed from these two–phase data. For the relative permeabilities Stone's second method was used.[2,30] This yields the relative permeabilities for the water and gas phases as the two–phase functions of the corresponding saturations. The intermediate wetting phase – NAPL – relative permeability after Stone is given by the following representation:

$$k_{rn}^* \quad = \quad k_{rncw} \quad [(k_{rnw}/k_{rncw} + k_{rw})\;(k_{rng}/k_{rncw} + k_{rg}) - (k_{rw} + k_{rg})] \tag{26}$$

k_{rnw} is the NAPL relative permeability in a NAPL–water system, k_{rng} denotes the NAPL relative permeability in a gas–NAPL system in the presence of water at residual saturation. k_{rncw} is the NAPL relative permeability in the water–NAPL two–phase system at water residual saturation. The following modification to (26)

$$k_{rn} = \max\,(k_{rn}^*, 0) \tag{27}$$

guarantees that the NAPL relative permeability assumes only non–negative values.

The pressure dependent functions are given as follows:

$$\phi \quad = \quad \phi^0\,(1 + \beta_s\,(\bar{p} - p^0)) \tag{28}$$

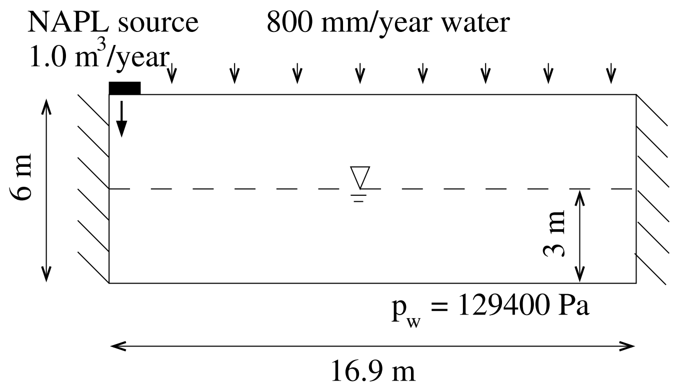

Figure 9: 3D–NAPL infiltration: Configuration

$$\rho_\alpha = \rho_\alpha^0 (1+\beta_\alpha (p_\alpha - p^0)), \quad \alpha \in \{w,n\} \tag{29}$$
$$\rho_g = M_g p_g/(RT) \tag{30}$$

The ideal gas law is used for the compressibility of the air phase. p^0 in the equations above is the atmospheric pressure $(p^0 = 10^5 Pa)$, $M_g = 14.05 mole/m^3$ is the molecular weight of air, $R = 8.314 J/(mole K)$ is the universal gas constant, and absolute temperature T is taken as $T = 288K (= 15^o C)$. $\bar{p}$ is the average pressure of the system which is defined by

$$\bar{p} = p_w S_w + p_n S_n + p_g S_g \quad . \tag{31}$$

The model domain is discretized with rectangular elements of dimension:

$$\Delta x_i = 2.0^{(i/2)} m \quad , \ i = 0, \cdots, 5, \qquad \Delta z = 0.25 m \quad . \tag{32}$$

The choice of horizontal discretization lengths provides an accurate approximation of the pressure gradients and velocities, i.e., their approximations are independent of the distance to the contaminant source.

In contrast to the problem of Faust (1985) and Panday et al. (1994) the unsaturated zone is almost entirely at residual water saturation.[8,24] This comes from the use of different constitutive relationships. Furthermore, they had a shallow water table only 1.5 m below the surface level and they employed the passive air phase assumption which neglects pressure gradients in the air phase.

In this simulation the full three–phase formulation as described in Section 3 is used. The initial time step is 1000 s. An aggressive time step selector is employed. A maximum time step of 10 days is chosen.

The infiltration problem is done for two cases. First the density properties of tetrachloroethylene (TCE) (see Tab. 7) are assumed for the NAPL. TCE is denser than water and gravity effects are expected to dominate the propagation behavior.

Figures 10 to 13 show the saturation distributions at four different times over a period of 5 years as predicted by the three–phase simulator *box3p3c*.

The penetration of the unsaturated zone by the infiltrating DNAPL is characterized by the large density differences between soil air and DNAPL. Capillary effects are much smaller.

Table 7: Parameter values for the infiltration problem

Parameter	Symbol	Unit	Value
Permeability	$\mathbf{K}$	m^2	10^{-12}
Porosity*	ϕ^0	–	0.3
Water density*	ρ_w^0	$kg\,m^{-3}$	1000
DNAPL density*	ρ_n^0	$kg\,m^{-3}$	1460
LNAPL density*	ρ_n^0	$kg\,m^{-3}$	950
Air density*	ρ_g^0	$kg\,m^{-3}$	1.25
Water viscosity	μ_w	$kg\,m^{-1}\,s^{-1}$	10^{-3}
NAPL viscosity	μ_n	$kg\,m^{-1}\,s^{-1}$	10^{-3}
Air viscosity	μ_g	$kg\,m^{-1}\,s^{-1}$	$2 \cdot 10^{-5}$
Water compressibility	β_w	Pa^{-1}	$4.3 \cdot 10^{-9}$
NAPL compressibility	β_n	Pa^{-1}	$3.0 \cdot 10^{-9}$
Porous medium compressibility	β_s	Pa^{-1}	10^{-10}

* : at atmospheric pressure $p^0 = 10^5 Pa$.

As a result DNAPL propagates almost completely in the vertical downward direction. After 168 days, the DNAPL plume reaches the water table at a depth of 3.0 m. After 684 days, DNAPL has reached the draining aquifer at the bottom of the model domain (see Fig. 10). A gradual but small horizontal expansion of the DNAPL plume is observed over the entire vertical range. Fig. 11 shows the phase saturations along a vertical line through the NAPL source. At the beginning of the NAPL infiltration the DNAPL plume displaces air. This displacement takes place mainly in horizontal direction. The DNAPL plume is accompanied by a small water front. After about 500 days the saturation profiles along the vertical axis do not change significantly. The DNAPL saturations above the water table assume a uniform distribution of 0.20, and below the water table they have a level of 0.10.
The same numerical simulation is done for a LNAPL with a density of 950 kg/m^3 (see Tab. 7). The LNAPL behaves in the unsaturated zone similarly to the DNAPL. Gravity forces are here the dominating propagation mechanism. After 250 days the LNAPL plume gets into contact with the saturated zone. Now, a pooling of LNAPL along the water table takes place. At this depth a significant horizontal movement of NAPL away from the contaminant source is observed. According to the numerical simulation, this LNAPL plume has reached after an infiltration period of 5 years a distance of more than 7 m from the LNAPL source. In the center of the LNAPL pool (see Fig. 13) maximum LNAPL saturations of 0.23 are predicted by the numerical simulation. The saturation profiles along the vertical axis through the contaminant source are during the passage of the plume through the vadose zone similar to the DNAPL. However, after reaching the water table the plume propagates very slowly further downwards. The water table below the infiltration zone is pushed gradually downwards by the weight of the pooling LNAPL.
Both scenarios, LNAPL and DNAPL infiltrations, cause long term contamination sources for the groundwater. Solution processes from the pooled or residual NAPL phase into the flowing groundwater and soil air take place very slowly over a long period of time.
In contrast to the infiltrated DNAPL phase LNAPL accumulates in the unsaturated zone. Thus,

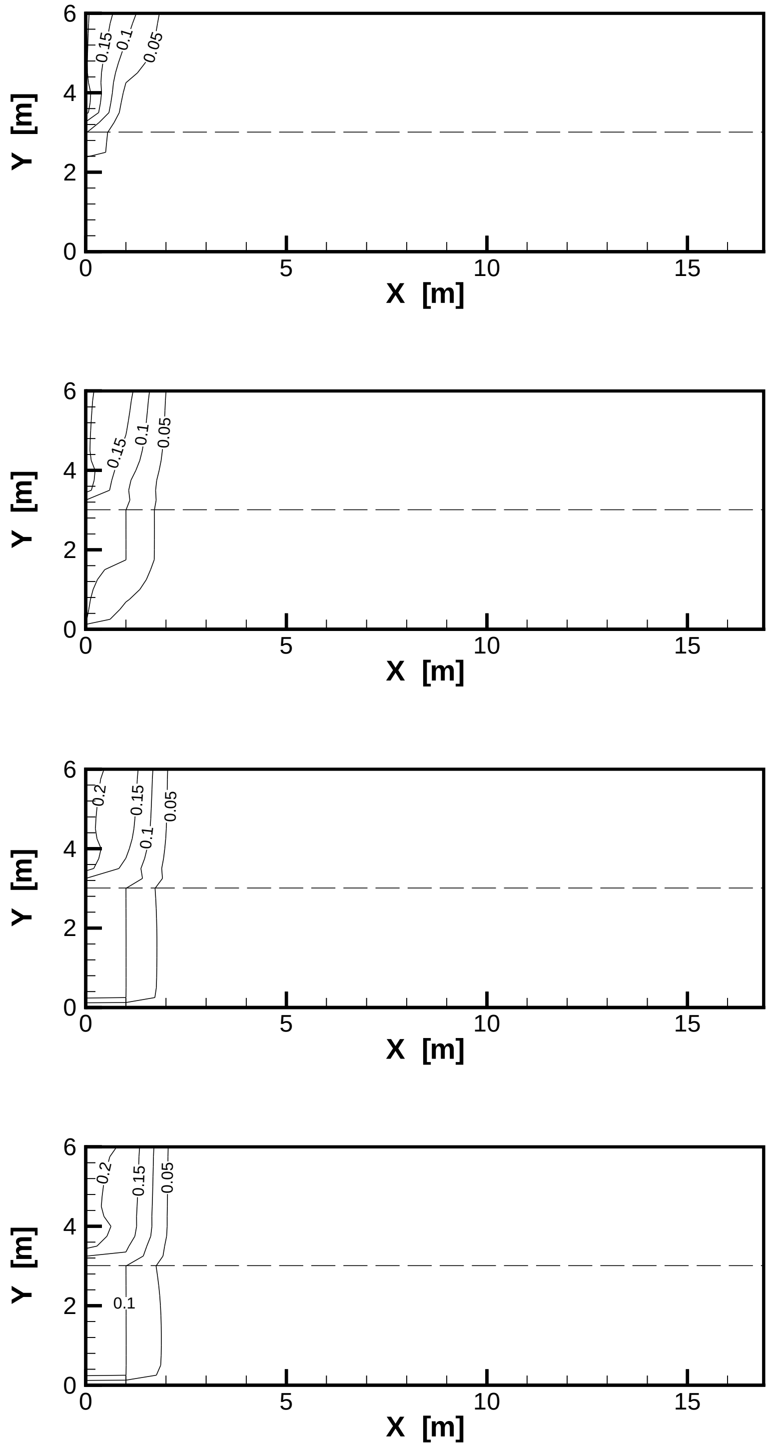

Figure 10: Predicted DNAPL saturations after 227, 684, 1243, 1830 days of infiltration

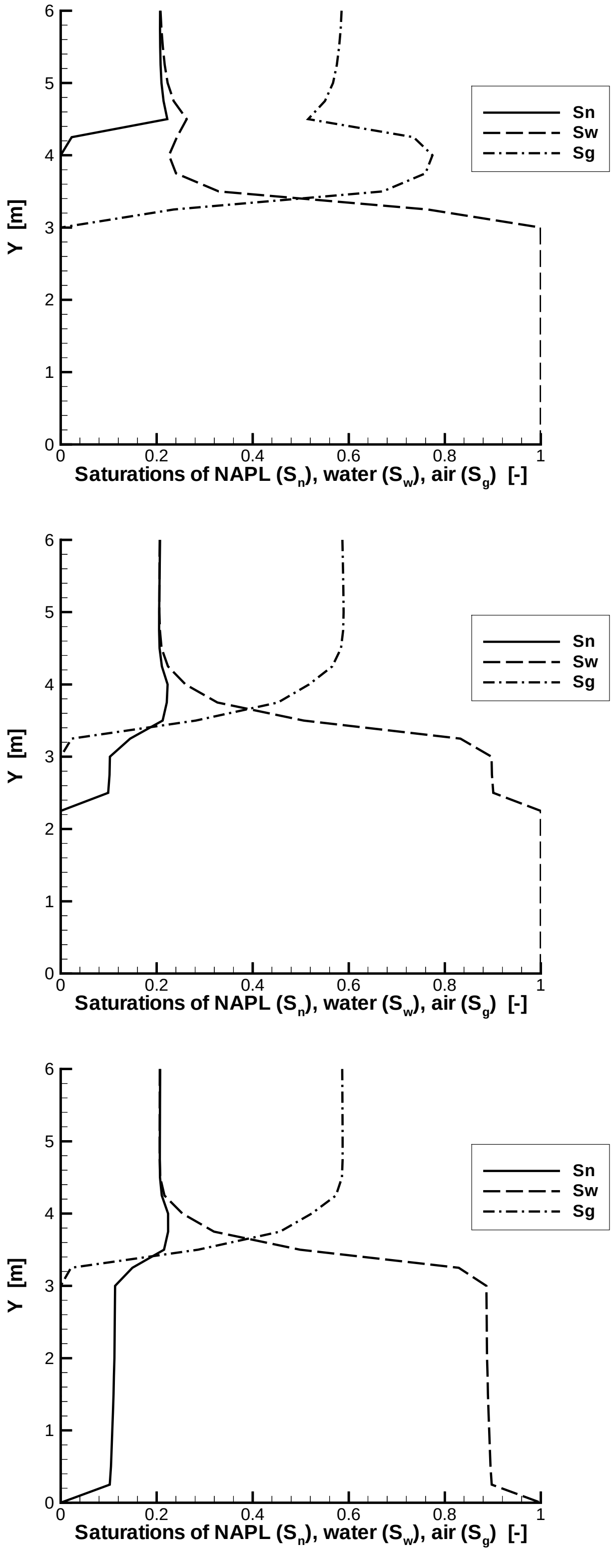

Figure 11: Predicted phase saturations below the infiltration zone after 60, 227, and 684 days

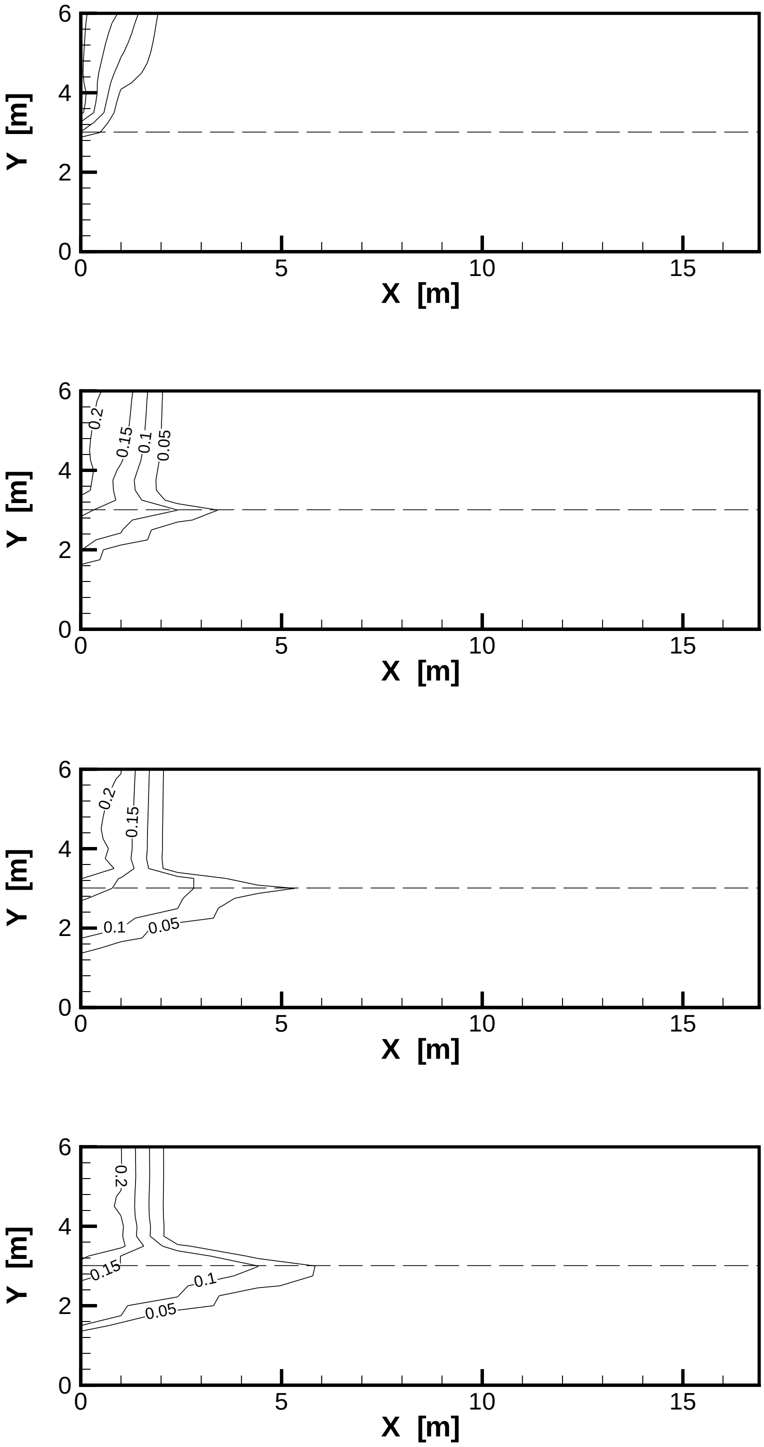

Figure 12: Predicted LNAPL saturations after 250, 727, 1314, 1883 days of infiltration

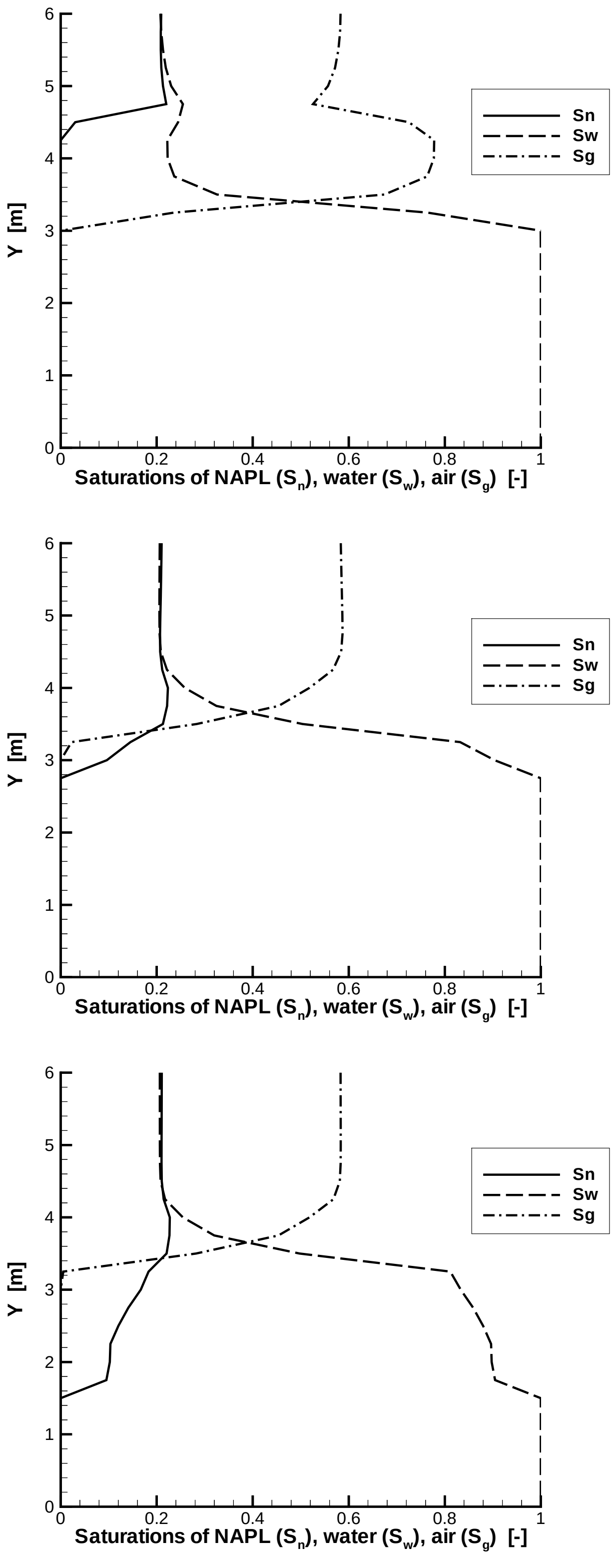

Figure 13: Predicted phase saturations below the infiltration zone after 59, 250, and 727 days

LNAPL contaminations are easier to assess and clean–up strategies such as excavation or other in–situ remediation techniques can be applied.

Table 8: Runtime statistics (simulation of 1800 days)

Problem	Parameter	Unit	Formulation	
			*box*3*p*	*box*3*p*3*c*
DNAPL problem:				
	Total cpu time*	s	1881	2505
	No. of time steps	-	407	383
LNAPL problem:				
	Total cpu time*	s	1419	1841
	No. of time steps	-	371	374

* : on a Pentium MMX 233 MHz.

To demonstrate the computational efficiency of the numerical formulations runtimes for the two problems are listed in Table 8. The *box*3*p* formulation is in all cases faster than *box*3*p*3*c*. However, *box*3*p* did not converge for all initial saturations to the equilibrium state at the beginning of the infiltration problem. Furthermore, assigning the saturated zone nodes initially values of $S_w = 1.0$ leads to a breakdown of the *box*3*p* simulation after the NAPL front reaches the water table. This is the case for both, DNAPL and LNAPL. *box*3*p*3*c* shows no convergence problems for such changes in the phase state, although convergence in general is slower. This problem with *box*3*p* is fixed by assigning initial water saturation values to the saturated zone nodes which are slightly below one. Then the *box*3*p* formulation gives correct simulation results and shows better convergence than *box*3*p*3*c*.

6 DISCUSSION AND CONCLUSIONS

Two– and three–dimensional three–phase flow problems for groundwater contamination, as well as other applications such as reservoir engineering, were presented. The numerical simulators give stable solutions for a wide range of problems. Both formulations coincide in the special case of full three–phase flow domains. However, in some cases the variable substitution algorithm of $box3p3c$ shows a more robust behavior but slower convergence than $box3p$. The numerical results of the verification problem in Section 4 show that the highest oil production is achieved for large initial oil saturations (case 2). For smaller initial oil and higher water saturations the production rate of oil diminishes (case 4).

The numerical simulation of LNAPL infiltrations in Sections 5.1 and 5.2 show that LNAPL pools up above the water table and starts migrating in lateral direction. In 5.1 the problem was two–dimensional with an inclined water table. The results indicate that most LNAPL moves downstream. However, a small portion of LNAPL migrates upstream due to capillary forces. This is in accordance with several observations at laboratory experiments, in the field, or at sites of accidental spills.

In the three–dimensional problem in Section 5.2 the different propagation behavior of LNAPL and DNAPL is studied. The selected configuration resembles partly the one from Faust (1985).[8] Faust used almost linear air relative permeability and air–NAPL capillary pressure functions. Furthermore, he simulated a shallow aquifer. This results in an initial unsaturated zone with water saturations of 0.85 and higher. This means, he simulated relatively wet conditions in the unsaturated zone. As a consequence, LNAPL migrates at very small depths in lateral direction. In contrast to this, here, different constitutive relationships are used which are taken from Forsyth (1991). These relations yield a vadose zone which is almost entirely at residual water saturation, although a higher water recharge is assumed. Thus, the propagation behavior of LNAPL in the vadose zone is different to the one in Faust's problem. LNAPL moves vertically downwards until it reaches the water table. As a conclusion to this, the water saturations in the unsaturated zone are sensitive to the constitutive relationships used. Dependent on them the simulated migration of LNAPL can differ considerably.

The constitutive relations have a major impact on the numerical results. One conclusion of the present investigation is that an accurate simulation of a real contamination scenario requires very good and detailed knowledge of the soil characteristics. Other investigatons (e.g., Croisé et al.[6]) support this conclusion.

The DNAPL migration in Faust's problem and in the presented example are similar. DNAPL moves due to gravitational forces almost exclusively downwards. However, the saturation levels in the vadose zone are higher than in the saturated zone.

Multiphase flow simulators cannot describe the solution of NAPL components in the surrounding soil air and groundwater, and their migration in the aquifer. Due to their circulation contaminant substances can propagate much faster in these phases than in their orginial NAPL phase. Taking account for such solution and transport processes requires a compositional model. $box3p3c$ is a basis for such a compositional simulator. A flash calculation which uses the assumption of a local thermodynamic equilibrium can be integrated in the present variable substitution algorithm.

ACKNOWLEDGEMENTS

Funding for the research described in this article was provided by Deutsche Forschungsgemeinschaft, SFB 404 'Mehrfeldprobleme in der Kontinuumsmechanik'. The first author is supported by the foundation "Besinnung und Ordnung".

References

[1] T. Arbogast, M.F. Wheeler, & I. Yotov. Mixed finite elements for elliptic problems with tensor coefficients as cell–centered finite differences. *SIAM J. Num. Anal.*, **34** (1997) 1 – 28.

[2] K. Aziz & A. Settari. *Petroleum Reservoir Simulation*. Applied Science Publ. Ltd., London, 1979.

[3] J.B. Bell, J.A. Trangenstein, & G.R. Shubin. Conservation Laws of Mixed-Type describing Three-Phase Flow in Porous Media. *SIAM J. Appl. Math.*, **46** (1986) 1000 – 1017.

[4] S.E. Buckley & M.C. Leverett. Mechanism of Fluid Displacements in Sands. *Transactions of the AIME*, **146** (1942) 107 – 116.

[5] G. Chavent & J. Jaffré. *Mathematical models and finite elements for reservoir simulation*. North Holland, Amsterdam, 1986.

[6] J. Croisé, H. Sheta, & R. Helmig. Numerische Modellierung von NAPL-Infiltrationsvorgängen in Lockergesteinen. Technical Report 95/1 (HG 214), Institut für Wasserbau, Universität Stuttgart, 1995.

[7] R.W. Falta, K. Pruess, I. Javandel, & P.A. Witherspoon. Numerical modeling of steam injection for the removal of nonaqueous phase liquids from the subsurface 2. code validation and application. *Water Res. Res.*, **28** (1992) 451–465.

[8] C.R. Faust. Transport of Immiscible Fluids Within and Below the Unsaturated Zone: A Numerical Model. *Water Res. Res.*, **21** (1985) 587 – 596.

[9] P.A. Forsyth. Adaptive implicit criteria for two–phase flow with gravity and capillary pressure. *SIAM J. Sci. Stat. Comp.*, **10** (1989) 227–252.

[10] P.A. Forsyth. A control volume finite element approach to NAPL groundwater contamination. *SIAM J. Sci. Stat. Comp.*, **12** (1991) 1029 – 1057.

[11] P.A. Forsyth. A positivity preserving method for simulation of steam injection for NAPL site remediation. *Adv. Water Res.*, **16** (1993) 351–370.

[12] P.A. Forsyth & B.Y. Shao. Numerical simulation of gas venting for NAPL site remediation. *Adv. Water Res.*, **14** (1991) 354 – 367.

[13] B.S. Gottfried, W.H. Guilinger, & R.W. Snyder. Numerical Solution of the Equations for One–Dimensional Multi–Phase Flow in Porous Media. *SPE J.*, **6** (1966) 62–72.

[14] F.G. Helfferich. Theory of multicomponent, multiphase displacement in porous media. *SPE J.* (1981) Febr. 51–62.

[15] R. Helmig. *Multiphase Flow and Transport Processes in the Subsurface – A Contribution to the Modelling of Hydrosystems*. Springer, Heidelberg, Berlin, 1997.

[16] R. Helmig & R. Huber. Comparison of different Galerkin–type discretization techniques for two–phase flow in porous media. *Adv. Water Res.*, (to appear) .

[17] M. Honarpour, L. Koederitz, & A.H. Harvey. *Relative Permeability of Petroleum Reservoirs*. CRC Press, Inc., Boca Raton, Fla., 1986.

[18] R. Huber. Kopplung von FE–/FV–Methoden zur numerischen Simulation von Zweiphasenströmungen in heterogenen, porösen Medien. Master's thesis, Institut für Wasserbau, Univ. Stuttgart, 1995.

[19] R. Huber & R. Helmig. Multiphase Flow in Heterogeneous Porous Media: A classical Finite Element Method versus an IMPES–based mixed FE/FV approach. *J. Num. Meth. Fluids*, (to appear) .

[20] A.A. Keller, M.J. Blunt, & P.V. Roberts. Micromodel observation of the role of oil layers in three–phase flow. *Trans. Porous Media*, **26** (1997) 277–297.

[21] B.H. Kueper & E.O. Frind. Two–Phase Flow in Heterogeneous Porous Media 1. Model Development. *Water Res. Res.*, **27** (1991) 1049–1057.

[22] B.H. Kueper & E.O. Frind. Two–Phase Flow in Heterogeneous Porous Media 2. Model Application. *Water Res. Res.*, **27** (1991) 1059–1070.

[23] J.E. McCray & R.W. Falta. Numerical Simulation of Air Sparging for Remediation of NAPL Contamination. *Groundwater*, **35** (1997) 99–110.

[24] S. Panday, Y.S. Wu, P.S. Huyakorn, & E.P. Springer. A three–dimensional multiphase flow model for assessing NAPL contamination in porous and fractured media, 2. Porous medium simulation examples. *J. Cont. Hydrol.*, **16** (1994) 131–156.

[25] J.C. Parker. Multiphase Flow and Transport in Porous Media. *Reviews of Geophysics*, **27** (1989) 311 – 328.

[26] D.W. Peaceman. *Fundamentals of Numerical Reservoir Simulation*. Elsevier, Amsterdam, 1977.

[27] L.A. Richards. Capillary conduction of liquids in porous media. *Physics*, **1** (1931) 318–333.

[28] H. Sheta, R. Huber, J. Braun, & R. Helmig. Infiltration and Remobilisation of DNAPL in Heterogeneous Aquifer Systems – Comparison of Experimental and Numerical Results. *Water Res. Res.*, (in preparation) .

[29] B.E. Sleep & J.F. Sykes. Compositional Simulation of Groundwater Contamination by Organic Compounds: 1. Model Development and Verification. *Water Res. Res.*, **29** (1993) 1697 – 1708.

[30] H.L. Stone. Estimation of three–phase relative permeability and residual oil data. *J. Can. Pet. Technol.*, **12** (1973) 53–61.

[31] H.J. Welge. A Simplified Method for Computing Oil Recovery by Gas and Water Drive. *Transactions of the AIME*, **195** (1952) 91–98.

APPENDIX

Table 9: Relative permeability and capillary pressure data for the two–phase NAPL–water (nw) system[11]

S_w	k_{rw}	k_{rnw}	p_{cnw} $[Pa]$
0.2	0.00	0.68	9000
0.3	0.04	0.55	5400
0.4	0.10	0.43	3900
0.5	0.18	0.31	3300
0.6	0.30	0.20	3000
0.7	0.44	0.12	2700
0.8	0.60	0.05	2400
0.9	0.80	0.00	1500
1.0	1.00	0.00	0

Table 10: Relative permeability and capillary pressure data for the two–phase air–NAPL (gn) and air–water (gw) systems[11]

S_g	k_{rng}	p_{cgn} $[Pa]$	p_{cgw} $[Pa]$
0.00	0.68	0	0
0.05	0.58	500	500
0.10	0.49	900	1000
0.20	0.34	1200	2000
0.30	0.21	1500	3000
0.40	0.116	1800	3300
0.50	0.045	2100	3600
0.60	0.0009	2400	3900
0.68	0.0	3000	4500
0.80	0.0	9000	6000